Development of 3D Fused Quartz Hemi-Toroidal Shells for High-Q Resonators and Gyroscopes

Mohammad H. Asadian , *Student Member, IEEE*, Yusheng Wang , *Student Member, IEEE*, and Andrei M. Shkel, *Fellow, IEEE*

Abstract—In this paper, recent developments in the design and fabrication of micromachined fused quartz hemi-toroidal shells are presented. The fabrication is based on micro glassblowing process, demonstrated to enable the realization of high-Q MEMS resonators and gyroscopes. The design optimization of the shell geometry is performed using parametric finite element analysis. The effect of geometric parameters on the scaling of the resonant frequencies and energy dissipation are discussed. Three variations of the micro-glassblowing process are studied in the paper, concluding that shell resonators with a broad operational frequency range without losing the symmetry and Q-factor are feasible. Finite element models are presented to simulate the presented glassblowing processes, which are used to predict the final geometry of shell resonators accurately. Operational frequency as low as 5 kHz and Q-factor as high as 1.7 million is demonstrated on the fabricated shell resonators. The proposed process modifications demonstrate a low-cost and scalable fabrication of 3D shells for resonators and gyroscopes, which can be used in inertial navigation and timing applications.   [2019-0179]

Index Terms—3D MEMS, fused quartz, fabrication, resonators, gyroscopes.

I. INTRODUCTION

3D Fused Quartz (FQ) shells offer mass, stiffness, and damping symmetry, as well as structural rigidity, for the sensing element of Coriolis Vibratory Gyroscopes (CVG). A precisely machined and polished hemispherical shell is the core of a Hemispherical Resonator Gyroscope (HRG) [1]. The outstanding performance of HRG has originated from its highly symmetric hemispherical structure with an extraordinarily Q-factor (> 25 million), and has motivated the development

M. H. Asadian is with the Microsystems Laboratory, Department of Mechanical and Aerospace Engineering, University of California at Irvine, Irvine, CA 92697 USA (e-mail: asadianm@uci.edu).

Y. Wang is with the Microsystems Laboratory, Department of Mechanical and Aerospace Engineering, University of California at Irvine, Irvine, CA 92697 USA (e-mail: yushengw@uci.edu).

A. M. Shkel is with the Microsystems Laboratory, Department of Mechanical and Aerospace Engineering, Department of Electrical Engineering and Computer Sciences, University of California at Irvine, Irvine, CA 92697 USA, and also with the Department of Biomedical Engineering, University of California at Irvine, Irvine, CA 92697 USA (e-mail: ashkel@uci.edu).
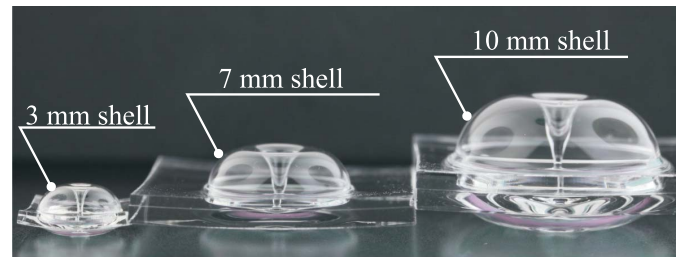
Fig. 1. Fused quartz 3D shells with different geometries, fabricated using the high-temperature micro-glassblowing process.

of batch fabrication and miniaturization of 3D shell resonators, utilizing Micro-Electro-Mechanical Systems (MEMS) fabrication techniques.

The fabrication processes to realize MEMS-based 3D resonators and gyroscopes can be classified into two main categories: (1) thin-film shell resonators and (2) bulk-deformed shell resonators. In the former, thin film structural and sacrificial materials are deposited on pre-etched hemispherical cavities or precision microspheres, and the shell resonators are released by removal of the sacrificial material. Polysilicon [2], silicon dioxide [3], Ultra-Low Expansion (ULE) glass [4], microcrystalline diamond [5], and an Iron-Nickel alloy (Invar) [6] were used as the structural material for thin-film shell resonators. The thickness of thin-film shell resonators was limited by the maximum thickness allowance to achieve a low-stress thin-film deposition, hence, it was limited to just a few microns. The bulk-deformed shell resonators were fabricated based on a high-temperature thermo-plastic deformation of the structural materials, such as borosilicate glass [7]–[9], Bulk Metallic Glass (BMG) [10], [11], ULE glass [12], and Fused Quartz (FQ) [13]–[15].

Micro-glassblowing process was initially developed for wafer-level fabrication of microspherical glass cells for nuclear magnetic resonance (NMR) atomic sensors [16]–[18]. In this process, a cavity was etched using Deep Reactive Ion Etching (DRIE) in a silicon substrate wafer, and encapsulated by silicon-to-glass anodic wafer bonding. At the glassblowing temperature (∼ 850 °C), the pressure builds up inside the encapsulated cavity while simultaneously the viscosity of glass decreases. The viscous glass layer expands, while the surface tension force minimizes the surface area and forms 3D spherical shells. The process was adapted for the fabrication of microspherical [8], [19], [20] and inverted wineglass [7] shell resonators. In the FQ glassblowing process,
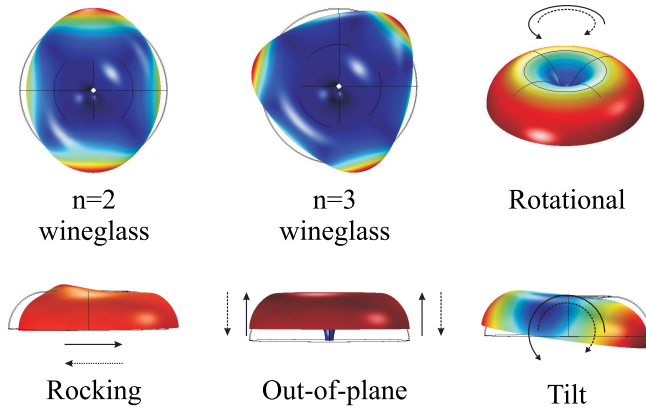
Fig. 2. The first six resonance modes of a typical hemi-toroidal shell structure, any degenerate wineglass modes can be used for rotation sensing, however the n=2 mode is preferable due to a higher gain in the whole angle mode of operation.
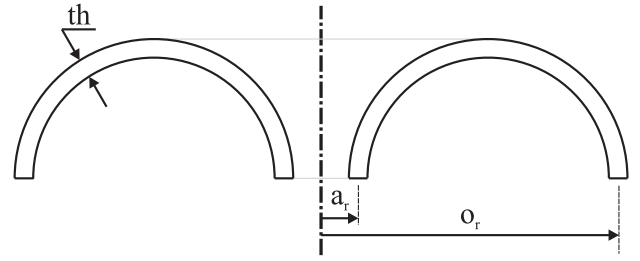

Fig. 3. Schematics of cross-section of a hemi-toroidal shell used in the parametric FE simulations for frequency scaling analysis. The anchor radius, a_r, shell outer radius, O_r, and the shell thickness, th are indicated on the cross-sectional view.

the cavities were etched in a FQ wafer and encapsulated by plasma-assisted FQ-to-FQ wafer bonding [13]. Since FQ has a higher softening temperature compared to borosilicate glass, the glassblowing occurs at temperatures greater than 1500 °C. Hemi-toroidal FQ shell resonators with a broad range of operational frequencies were fabricated using the high-temperature micro-glassblowing process [21]. Fig. 1 shows FQ shells with different geometries, fabricated using the micro-glassblowing process.

In this work, we report the design optimization and process developments for fabrication of high-Q FQ shell resonators with a broad range of operational frequencies.

In the following sections, we will discuss the design of shell resonators considering the scaling of operational, spurious resonant frequencies, and the energy dissipation through Thermoelastic Damping (TED), Section II. In Section III, we will discuss limitations of the baseline micro-glassblowing process and will present some alternative approaches to fabricate a wide range of shell geometries using modified version of the process. This will be followed by the finite element simulation of micro-glassblowing process for prediction of final shell geometry from the process parameters as an input, Section IV. The paper concludes with a demonstration of fabricated shell resonators with the designed frequency separation and mode ordering, validating the developed process for the design and fabrication of shells for high-Q gyroscopes, Section V.

II. DESIGN OF SHELL RESONATORS

In this section, the scaling of resonant frequency of operational and spurious vibrations modes with respect to the shell radius, thickness, and anchor radius are analyzed using the Finite Element (FE) modal analysis.

A. Scaling of Modal Resonant Frequency

Similar to any continuous structural systems with distributed mass and stiffness, such as beams, rings, plates, and membranes, a hemi-toroidal (or hemispherical) geometry has an infinite number of orthogonal modes of vibration. Fig. 2 shows six vibration modes of a typical hemi-toroidal shell,

anchored at its central stem. An input rotation along the axis of symmetry of shell resonators couples (any) degenerate wineglass modes through the Coriolis acceleration, and can be configured to detect the rotation rate (rate gyro) or the absolute angle of rotation (whole angle gyro). The n=2 wineglass mode is considered to be a preferable structural mode for operation due to a higher angular gain, which is a measure of sensitivity of the whole angle gyro.

The resonant frequency of the $n\theta$ wineglass modes of a hemi-toroidal shell was approximated analytically based on the Rayleigh's energy method [22]. In a hemi-toroidal shell with a uniform thickness, the wineglass frequency is linearly proportional to the thickness and inversely proportional to the square of the diameter. A parametric FE modal analysis was performed to derive the frequency scaling of the spurious modes. An FQ shell was approximated by a hemi-toroidal geometry for FE simulations. It was also assumed that the shell is fully developed to a hemi-toroidal shape and the thickness is uniform, Fig. 3. The scaling of resonance frequencies is plotted in Fig. 4. For a constant anchor radius and thickness, Fig. 4a, the frequency of all resonance modes decreases with increasing the shell radius. Fig. 4b shows the effect of shell's thickness on the resonance frequencies with a constant shell and anchor radius. It was observed that the order of resonance modes would switch at certain shell thicknesses (circled in Fig. 4b). A similar trend was observed with anchor radius, Fig. 4c. A larger anchor radius resulted in a higher torsional resonance frequency, while the wineglass and out-of-plane modes were nearly insensitive to size of the anchor. Similar trends were observed in other combinations of the shell radius, anchor radius, and thickness. The analysis of the FE modal simulation results reveal that:

- The resonance modes scale differently with respect to geometrical parameters of the hemi-toroidal shell;
- The frequency separation between the n=2 wineglass mode and spurious mode changed with shell geometry;
- The order of the resonance modes switched at certain geometries.

Based on the above observations, the different scaling of modal resonant frequencies would allow achieving a large frequency separation between the resonance modes and mode ordering, which would avoid the dissipation of energy through mode mixing [23], and thus mitigate the environmental sensitivity by avoiding low-frequency spurious resonance modes.
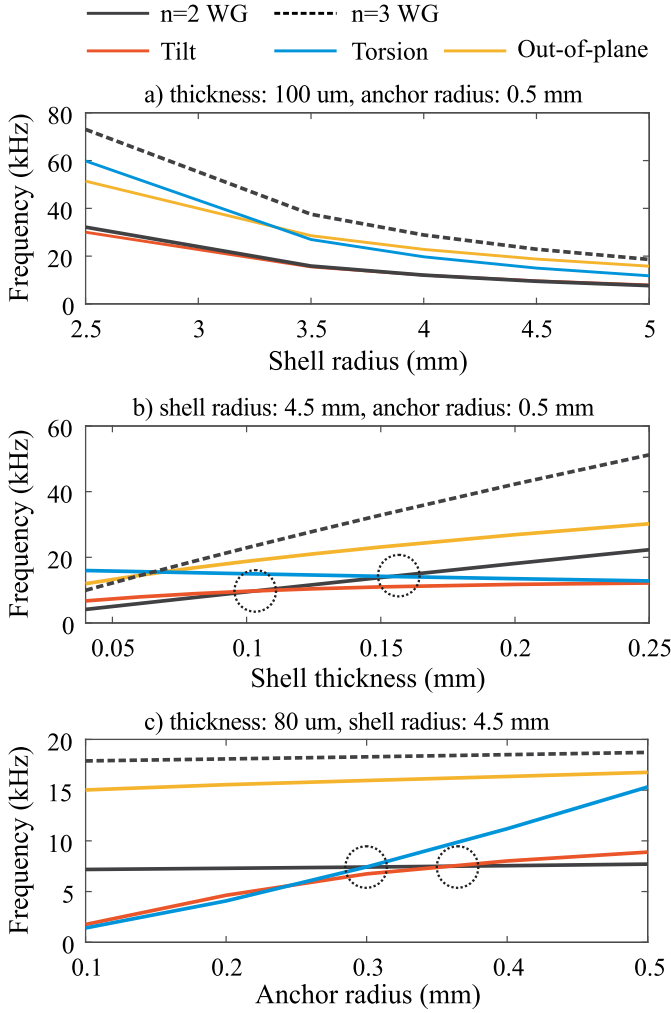
Fig. 4. Scaling of the resonance frequencies with respect to the geometry of hemi-toroidal shell resonators. Notice, the order of structural modes can switch at certain geometries. Circles indicate the geometries that the mode order of the n=2 wineglass mode and its closest spurious modes changes.

B. Effect of Shell Geometry on Modal Frequency Separation

The shell radius, thickness, and anchor radius are the design parameters that define the geometry of a hemi-toroidal shell. Using a series of parametric FE modal simulations, the shell thickness, radius, and anchor radius were varied from 40 μm to 150 μm, 2.5 mm to 5 mm, and 100 μm to 500 μm, respectively, generating more than 200 design combinations. The n=2 wineglass resonance frequency and the frequency separation with the closest parasitic mode at different design points were identified and plotted in Fig. 5. In this plot, each data point represents a distinct shell geometry, forming the design space for the geometry of hemi-toroidal shell resonators. The design space demonstrates that for a wineglass frequency of interest, a shell resonator can be obtained from a different combination of design parameters. Also, it indicates that separation between spurious and operational modes depends on selection of the geometric parameters. The result demonstrated a possibility of ordering the resonance modes of a shell resonator, with spurious modes at higher resonance frequencies, as compared to the frequency of the n=2 wineglass mode, which is an important consideration for avoiding the environmental excitation of the device during operation.
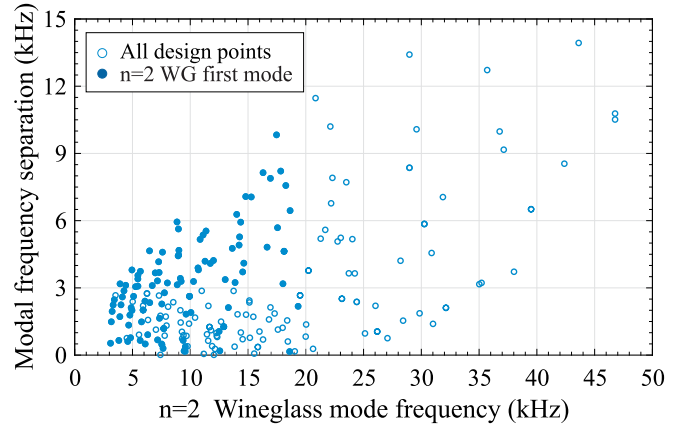

Fig. 5. The design space of hemi-toroidal shell resonators; frequency separation between the operational and the closest spurious modes at different n=2 wineglass resonance frequencies. Each data point represents a distinct shell geometry. The solid dots represent the mode-ordered design combinations where the n=2 wineglass is the lowest resonance mode.

The solid blue data points in Fig. 5 refer to cases where the mode-ordering condition is satisfied, and the n=2 wineglass mode has the lowest resonance frequency.

The trend of data points revealed that the modal frequency separation decreases at lower operational frequencies. Thus, at lower frequencies, the shell geometry should be optimized to avoid a proximity of spurious modes to the n=2 wineglass mode.

C. Effect of Shell Geometry on Thermoelastic Damping (TED)

The dissipation of energy through Thermoelastic Damping (TED) in resonators is due to non-reversible heat conduction in a solid medium, as a result of the coupling between the non-homogeneous strain fields and the temperature field within the vibration structure [24], [25]. The general expression of the TED based on Zener's model is,

$$Q_{TED}^{-1} = \left(\frac{E\alpha^2 T_0}{\rho C_p} \right) \sum_k f_k \frac{\omega \tau_k}{1 + (\omega \tau_k)^2} \qquad (1)$$

where, ρ is the density, C_p is the heat capacity at constant pressure, E is the Young's modulus, α is the coefficient of thermal expansion, T_0 is the equilibrium temperature, ω is the mechanical angular frequency, k denotes the number of thermal modes, f_k are the weights with $\sum f_k = 1$, and τ_k denotes the relaxation time constant to establish a temperature equilibrium across length b_k of different thermal modes,

$$\tau_k = \frac{b_k^2}{\pi^2 D} \qquad (2)$$

where D is the thermal diffusivity of the material.

The Q_{TED} of uncoated FQ shell resonators were calculated for the n=2 wineglass mode from FE simulations, using COMSOL Multiphysics. The Q_{TED} is plotted as a function of the n=2 frequency and as a function of thickness in Fig. 6, for the shell outer radius from 3 mm to 5 mm, and the shell thickness from 10 μm to 200 μm. Among all geometric parameters, thickness has the most significant effect on the TED in shell resonators [26]. For the range
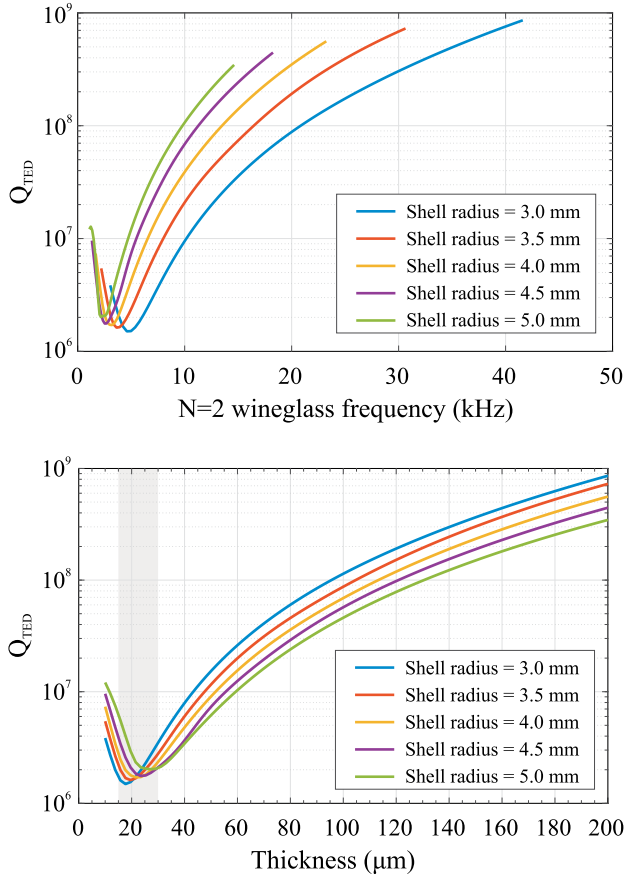
Fig. 6. Simulated Q_{TED} of uncoated hemi-toroidal shell resonators are plotted as a function of n=2 wineglass frequency (top) and as a function of shell thickness (bottom). The maximum dissipation was observed for the shell thickness in the range of 20 μm to 30 μm.

TABLE I
A SUBSET OF DESIGN COMBINATIONS FROM FIG. 5, CORRESPONDING TO n=2 WINEGLASS FREQUENCY $\sim$ 10 KHZ

Shell radius (mm)	Shell thickness (μm)	Anchor radius (mm)	n=2 Freq. (kHz)	Freq. separation (kHz)	Mode-ordered	Q-TED
3.5	60	0.6	10.21	3.2	Y	1.9E7
3.5	60	0.7	10.60	3.8	Y	1.9E7
4.0	80	0.6	10.02	1.9	Y	3.5E7
5.0	125	1.0	10.38	1.6	Y	8.1E7
5.0	150	0.3	10.84	4.4	N	1.6E8

a) Isotropic cavity etching in substrate wafer

b) Plasma-assisted FQ-to-FQ wafer bonding

c) Glassblowing at > 1500 °C

d) Substrate removal to release shell structures
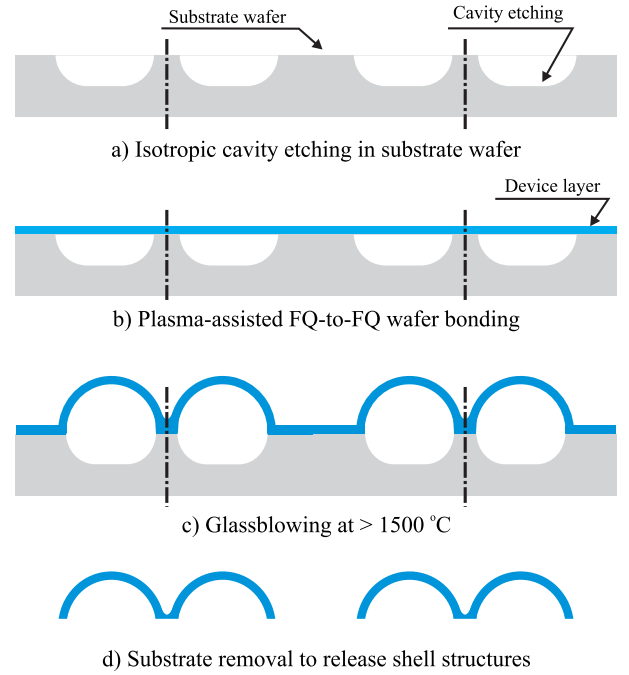
Fig. 7. The baseline micro-glassblowing fabrication process [13].

of studied parameters, the minimum Q-factor occurred when the thickness was between 20 μm and 30 μm, corresponding to the condition when the resonant frequency was between 2 kHz and 5 kHz. The quasi-isothermal condition in thinner shells and the quasi-adiabatic condition in thicker shells cause a weaker coupling between the strain field and the thermal field, reducing the energy dissipation through TED.

A lower operational frequency of shell resonators relaxes the minimum capacitive gap requirement for electrostatic frequency tuning when the shell resonator is instrumented to operate as a mode-matched gyroscope [27]. The design space was defined to select design parameters for low frequency shell resonators to increase the modal separation and achieve mode-ordering. The TED analysis was performed to avoid the design parameters that lead to maximum damping (lowest Q_{TED}). A set of parameters corresponding to design combinations with $\sim$ 10 kHz are listed in Table I. The modal frequency separation varies from 1.6 kHz to 4.4 kHz for the chosen set of parameters.

III. FABRICATION OF HEMI-TOROIDAL SHELL RESONATORS

A. Baseline Micro-Glassblowing Process

The high-temperature micro-glassblowing process was developed for fabrication of symmetric FQ wineglass resonators [13]. In the baseline process, annular cavities were etched on an FQ substrate wafer in a wet etching process using hydrofluoric (HF) acid (48 wt. % in water solution). The pre-etched substrate wafer was bonded to a blank FQ (or ULE) device wafer using the plasma-assisted wafer bonding under atmospheric pressure conditions. After dicing the bonded pair, the individual dies were transferred to a Rapid Thermal Processing (RTP) furnace, operating at a temperature above the softening point of the FQ ($>$1500 °C) for the glassblowing. Finally, the shell resonators were released from the substrate using the back-lapping and polishing process, Fig. 7. A shell resonator with the Q-factor of 1.1 million after metal coating and with an operational frequency of $\sim$ 100 kHz was demonstrated using the baseline process [13].

The glassblowing process has the transient and the steady-state thermal regimes. In the transient regime, when the die is placed into a furnace operating at $\sim$ 1550 °C, the die temperature increases until it reaches a steady-state condition. During the transient regime, the temperature is below the softening point of FQ and viscous deformation does not occur, hence, the volume of cavity does not change and the internal
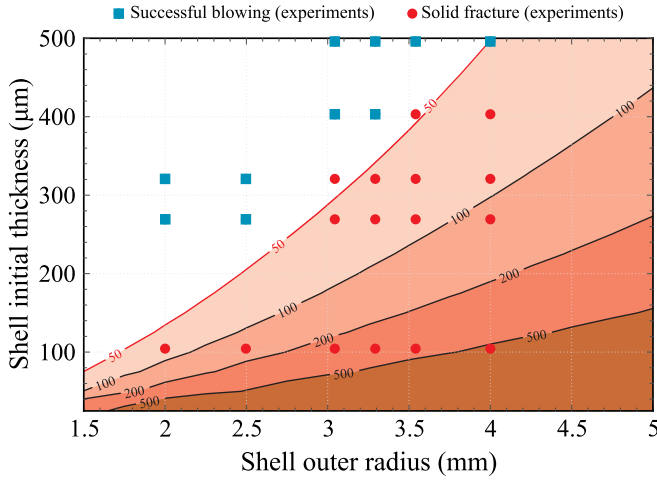
Fig. 8. Fracture limit of FQ shells before the viscous deformation due to exceeding the tensile strength of FQ (~50 MPa). The labels on dashed boundary lines indicate the stress level in MPa. Any combination of initial shell thickness and outer radius that results in regions with tensile stress level above 50 MPa would result in a solid fracture before glassblowing. The blue dots are the successful glassblowing experimentally, and red dots represent the failed glassblowing due to solid fracture.

pressure raises with temperature,

$$P_i = \frac{T_i}{T_{wb}} P_{wb}, \tag{3}$$

where P_i is the internal pressure inside the encapsulated cavity, T_i is the instantaneous temperature of the die, T_{wb} and P_{wb} are the temperature and pressure of the wafer bonding, respectively. The pressure induces tensile stresses in the solid FQ die. The maximum stress, σ_{max}, occurs at the edge of the encapsulated cavity where due to stress concentration,

$$\sigma_{max} = K_t \frac{(P_i - P_{gb})(r_2 - r_1)}{2 \, t_i}, \tag{4}$$

where K_t is the stress concentration factor, P_{gb} is the pressure inside the glassblowing furnace, r_1 and r_2 are the inner and outer radius of the pre-etched cavity, respectively, and t_i is the initial device wafer thickness. The maximum stress is proportional to shell radius and inversely proportional to the shell initial thickness. A stationary solid mechanics FE model was utilized to compute the maximum tensile stress on FQ dies. The pressure was calculated from Eq. 3 for T = 1100 °C and applied to the inner surface of cavity. The temperature-dependent properties of FQ were obtained from COMSOL Multiphysics material library. The FE results revealed that the maximum of stress at the location of stress concentration, a sharp edge of the encapsulated cavities, would exceed the tensile strength of the FQ material, ~50 MPa in some cases, resulting in the fracture of FQ layer before the onset of the viscous deformation. Fig. 8 demonstrates the solid fracture map of FQ dies in the baseline micro-glassblowing process. The labels indicate the maximum stress for the given combination of FQ thickness and outer radius. The FE results revealed that solid fracture is more likely to occur in thinner and larger (in diameter) shells, limiting the fabrication of shell resonators using the baseline glassblowing process.
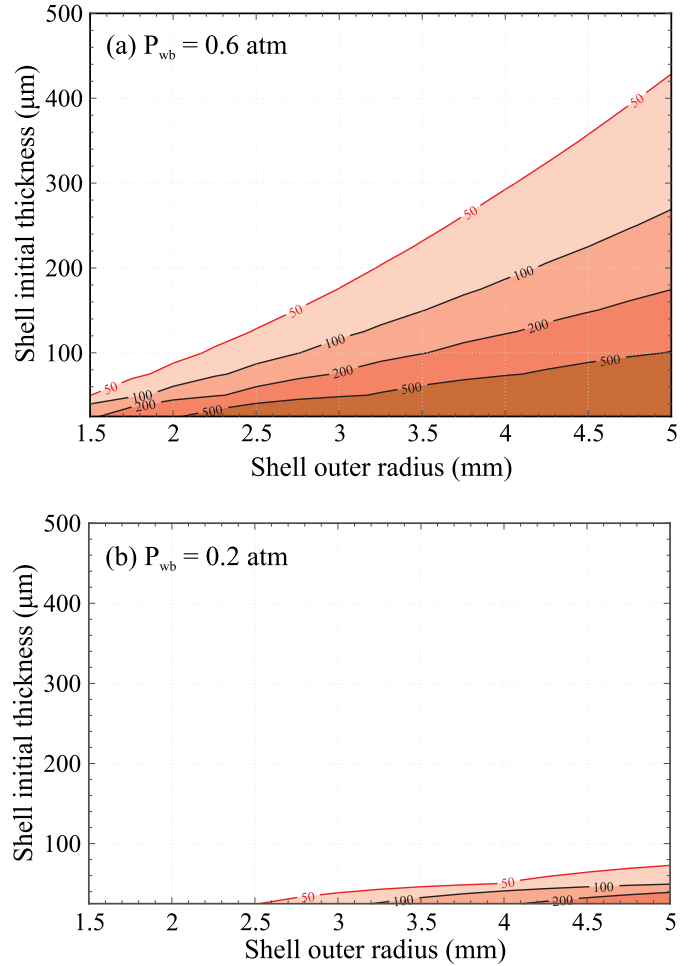

Fig. 9. FE simulation results of maximum stress in an FQ die bonded initially at (a) 0.6 atm and (b) 0.2 atm. The wafer bonding in a reduced pressure expands the safe design region of the shell geometry to avoid the solid fracture before the glassblowing.

B. Vacuum Micro-Glassblowing Process

The maximum stress during the transient thermal regime is directly proportional to the instantaneous pressure of the cavity, Eq. 4. The cavity pressure can be reduced by wafer bonding at a reduced pressure, $P_{wb} < 1$ atm, Eq. 3. The FE simulations were repeated for the reduced wafer bonding pressures. Fig. 9 shows the FE results for wafer bonding at 0.6 atm and 0.2 atm As expected, the lower wafer bonding pressure would reduce the maximum stress and expands the safe design region for the glassblowing process.

C. Reverse Micro-Glassblowing Process

Another approach to mitigate the maximum stress on the thin device layer during the glassblowing is to reduce the stress concentration. Fig. 10 shows the stress distribution in FQ dies, demonstrating local concentration of the tensile stress at the edge of encapsulated cavities. The concentration factor depends only on the geometry and it can be mitigated by reducing curvature at the sharp edges. The reverse glassblowing process takes advantage of the round edges formed during the isotropic wet etching of FQ wafers. In the reverse process,
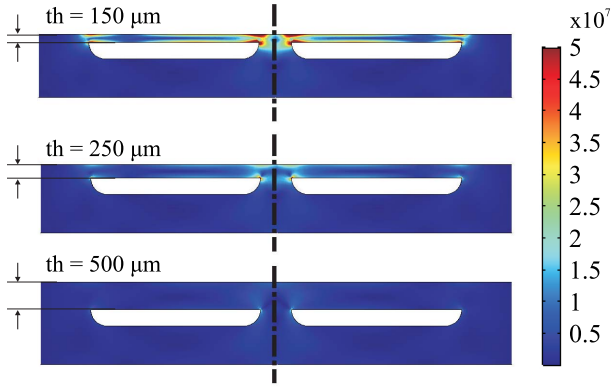
Fig. 10. Solid mechanics FE simulations reveal the localized concentration of stress on the edge of the encapsulated cavities which initiates cracks and breaks the FQ die in the baseline glassblowing process.
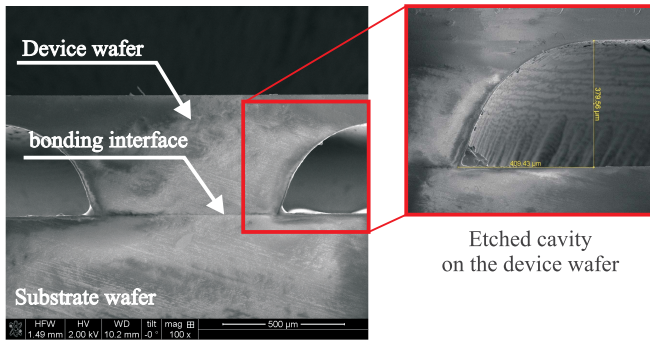

Fig. 11. Etch profile of a cavity on the device layer showing the round corners around the perimeter of the die on the thinner side.
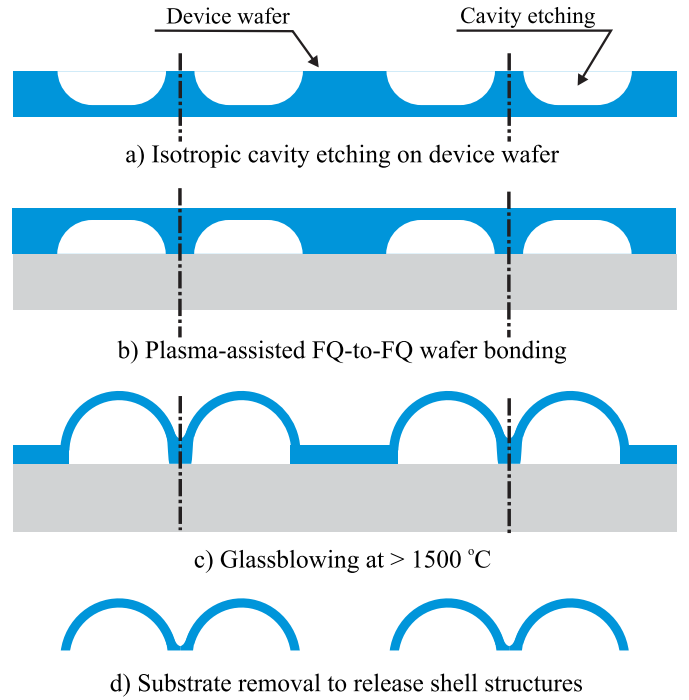

Fig. 12. The reverse micro-glassblowing fabrication process. The round edges on the thinner side of the cavity mitigates the fracture of FQ die before the glassblowing.
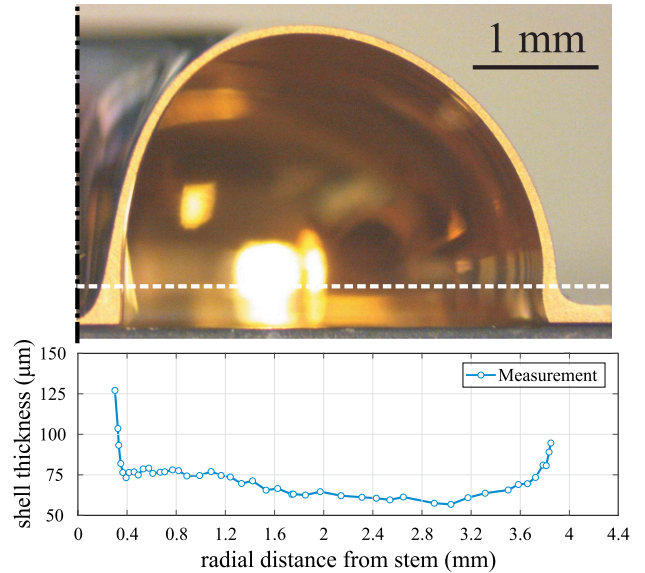

Fig. 13. Thickness measurement at the cross-section of an 8 mm glassblown shell with an initial thickness of 110 μm, due to different deformation rate, the top portion of the shell is ~30% thinner than the rim. (Note: the measurement data was obtained at the cross-section above the dashed white line).

the cavities were etched on the device wafer instead of the substrate wafer. The pre-etched device wafer was bonded to a blank substrate wafer using plasma-assisted wafer bonding. Fig. 11 shows a cross-section of an encapsulated die, illustrating the round corners on the thin side of the wafer. Unlike the baseline micro-glassblowing process, devices were glassblown from the cavity side, reducing the stress concentration due to the round edges formed by an isotropic wet etching, Fig. 12.

In general, for the footprint of devices in this study, shell resonators with higher operational frequencies, >50 kHz, can be fabricated using the baseline process, and the reverse process can be used for fabrication of lower frequency shell resonators, <25 kHz. The vacuum glassblowing process can be used to fabricate shell resonators in the frequency range between 25 kHz and 50 kHz.

IV. FINITE ELEMENT SIMULATION OF GLASSBLOWING PROCESS

The explored design space provides a set of parameters for the shell geometry at the operational frequency of interest. However, during the glassblowing process, the shell undergoes a severe deformation. Thus, it is crucial to determine the initial thickness of the fused quartz die before glassblowing, to achieve the intended final geometry. In addition, the thickness variation is inevitable in the glassblowing process. Because of the deformation gradient, the shell is thinner at the top and thicker around the rim area. Fig. 13 shows the thickness measurement at the cross-section of a glassblown shell with an initial thickness of 110 μm. The measurements revealed that the shell thickness at the rim is ~90 μm, but at the top is ~60 μm.

Although the shell thickness was assumed to be uniform in the parametric FE modal analysis, the design space provides

an insight into the shell geometry design optimization. For a more accurate estimation of the n=2 wineglass frequency and modal frequency separation, a model is developed to simulate the micro-glassblowing process and to predict the final geometry. The developed FE model captures the variation in the thickness; thus, provides more accurate information about the geometry of the glassblown shells.

The micro-glassblowing process was simulated with a Newtonian isothermal fluid flow model using COMSOL Multiphysics FE package. The temperature-dependent viscosity data were obtained from [28]. It was assumed that the die would reach the steady-state thermal condition. In this case, for simulating the glassblowing at 1550 °C, the FQ was modeled as a viscous material with viscosity and surface tension of 1.58×10^7 Pa.s and 0.295 N/m, respectively. The internal pressure was applied to the inner surface of the cavity. Assuming the steady-state isothermal condition, the change in the cavity volume due to shell viscous flow would change the internal pressure. As the shell deforms, the cavity volume, V_c, increases and the cavity internal pressure, P_c, drops consequently,

$$P_c = \frac{P_i V_{pc}}{V_c}, \tag{5}$$

where V_{pc} is the volume of the pre-etched cavity. The instantaneous volume of the cavity, V_c, was calculated at each time step of the simulation to re-calculate the internal pressure using Eq. 5. An automatic adaptive re-meshing technique was applied to limit the maximum mesh distortion and to ensure the mesh quality, as the fused silica layer undergoes large viscous deformations.

A. Baseline Micro-Glassblowing Process

In the baseline glassblowing process, a pre-etched substrate was bonded to a device wafer at atmospheric pressure and temperature, $P_{wb} = 1$ atm and $T_{wb} = 300$ K, resulting in an internal pressure of $P_i \sim 6.2$ atm (90 psi) at the beginning of the glassblowing. The pressure was applied on the inner surface of the cavity while the outer surfaces of the die (top and bottom) were subjected to atmospheric pressure. Due to the axial symmetry of the cavities, a 2D axisymmetric model was utilized for the simulations. Fig. 14 illustrates the applied boundary conditions of the FE model. The time-dependent cavity pressure, the shell height, and the backside blowing height are plotted as a function of simulation time in Fig. 15. The shell structure deforms until the pressure inside cavity reaches an equilibrium state with the furnace ambient pressure, P_{gb}, demonstrating the self-limiting nature of the micro-glassblowing process. The backside blowing would reduce the height of the device shell, and is inevitable in the glassblowing when the same material is used as the substrate and the device wafer. In this case, the backside blowing height is reduced when a thicker substrate wafer is used, inset in Fig. 15.

B. Vacuum Micro-Glassblowing Process

The height of a glassblown shell depends on the volume of the pre-etched cavity, V_{pc}, glassblowing temperature T_{gb},
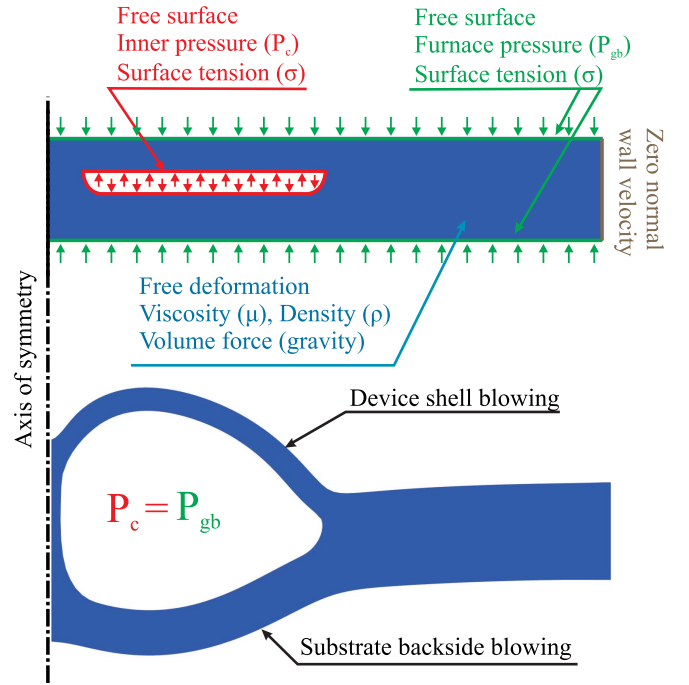

Fig. 14. Schematics of the FE model for simulation of glassblowing, indicating the applied boundary conditions and the resulting geometry.
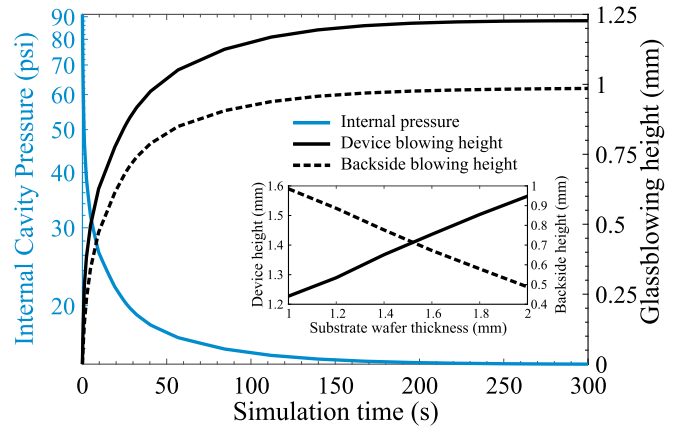

Fig. 15. Illustration of self-limiting characteristic of the micro-glassblowing process; as the pressure (solid blue line) drops and reaches an equilibrium state with the ambient, the shell deformation rate decreases and limits the shell height (solid black line). The backside of the substrate also blows (dashed black line). Inset figure shows that by using thicker substrate wafers, the backside blow reduces and the shell height increases. Simulations were performed for a 8 mm diameter shell with 500 μm initial thickness and 500 μm anchor radius.

wafer bonding pressure P_{wb}, and the glassblowing furnace pressure P_{gb}. In the vacuum micro-glassblowing process, the wafer bonding in partial vacuum mitigates the solid stress in a die. However, in the process it reduces the internal pressure of the cavity during the glassblowing, hence, reducing the height of the glassblown shell. The glassblowing in the vacuum would increase the pressure difference between the cavity and ambient, recovering the height of glassblowing. Fig. 16 illustrates the height of a shell with 200 μm thickness bonded under a reduced pressure, $P_{wb} = 0.6$ atm, at different furnace ambient pressures, P_{gb}. These results demonstrate that vacuum micro-glassblowing requires wafer bonding and glassblowing in a partial vacuum to fabricate FQ shell resonators.
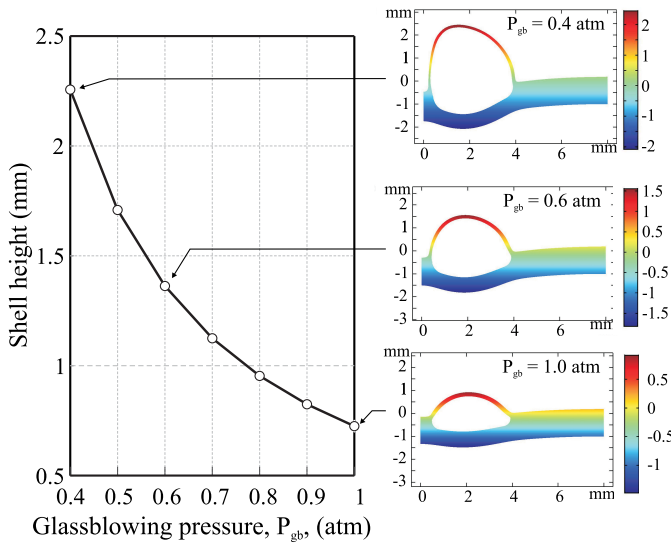
Fig. 16. Height of a 200 μm shell, bonded in a partial pressure (P_{wb} = 0.6 atm), under different ambient pressures. To fabricate fully developed shells, the glassblowing should be preformed at a reduced pressure in vacuum.

C. Reverse Micro-Glassblowing Process

The vacuum micro-glassblowing process reduces the maximum stress concentration and fracture of thin device layers at the cost of increased process complexity. The reverse process, enables fabrication of shell resonators without any requirements on controlling the wafer bonding pressure and glassblowing ambient. Fig. 17 demonstrates the shell height development in the reverse glassblowing process of a shell with an initial thickness of 100 μm and shell outer radius of 4 mm.

The initial thickness is determined from the wafer thickness and depth of etching. In one configuration, the device wafer with pre-etched cavities can be thinned using Chemical-Mechanical Polishing (CMP) to achieve the design initial thickness. In another configuration, the depth of etching can be controlled to achieve the design initial thickness. A broad range of thickness can be selected based on a combination of depth of etching and wafer thickness.

D. Post-Processing

The post-processing of the results of the fluid flow simulations was performed to reconstruct the 3D geometry of shell resonators. COMSOL Multiphysics was used for post-processing purposes. The results of the fluid flow at the final time step of the simulation were exported to the solid mechanics model. The 3D shell geometry was employed in further numerical simulations, such as modal analysis, estimation of TED and anchor loss, and transient dynamic analysis. The simulation results from modal analysis and TED are presented in the next section.

V. EXPERIMENTAL RESULTS

The standard grade Corning HPFS® 7980 wafers with an initial thickness of 500 μm were used for the fabrication of shell resonators. The wafers were time-etched to achieve
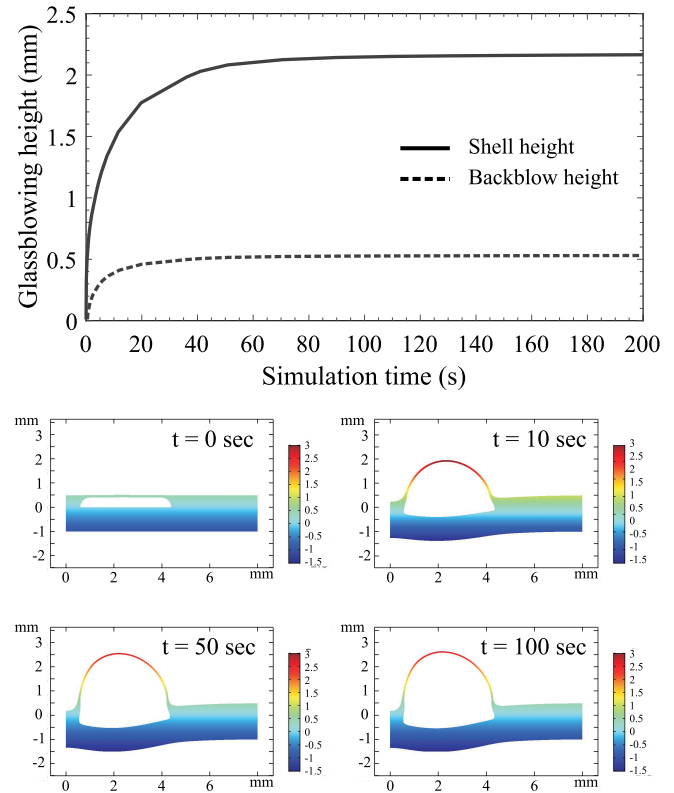

Fig. 17. Glassblowing height of a 200 μm shell bonded in a partial pressure (P_{wb} = 0.6 atm) under different furnace ambient pressures, P_{gb}. The glassblowing in atmospheric pressure would result in an under-blown shell. The height can be controlled by furnace pressure.
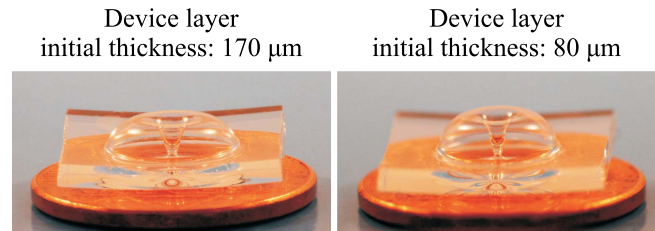

Fig. 18. 7 mm diameter shells with initial thicknesses of 170 μm and 80 μm were fabricated in the reverse glassblowing process.

different depths of etching and initial shell thicknesses. Fig. 18 shows 7 mm diameter shells, fabricated using the reverse glassblowing process with an initial thickness of 170 μm and 80 μm. The substrate was removed in a parallel back-lapping step using an Allied HighTech MultiPrep™ polisher. The bulk of substrate was removed using 30 μm and 15 μm diamond lapping film. The rim of the inner shell was polished using 3.0 μm OpTech™ slurry and 0.5 μm Cerium oxide suspension. The glassblown shell was mounted on a holder using Crystalbond™ 505 temporary adhesive. The adhesive supported the shell and protected it from chipping and cracking. After substrate removal, the adhesive was washed-away in a solvent bath and the shell was cleaned in a Piranha solution. Fig. 19 shows the steps of the substrate removal schematically. An Atomic Force Microscopy (AFM) measurement revealed surface roughness of 0.21 nm on the polished surfaces, Fig. 20.

1) Mount the shell using epoxy

2) Open the substrate by grinding, fill the inner cavity with epoxy

3) Grind the substrate and polish the rim

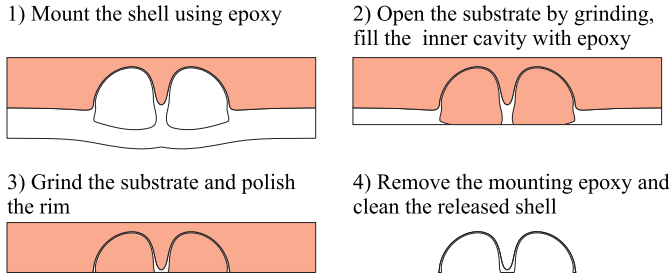4) Remove the mounting epoxy and clean the released shell

Fig. 19. Schematics of the substrate removal and polishing steps. The adhesive epoxy is necessary to support the inner and the outer surface of the thin shells to avoid cracking.
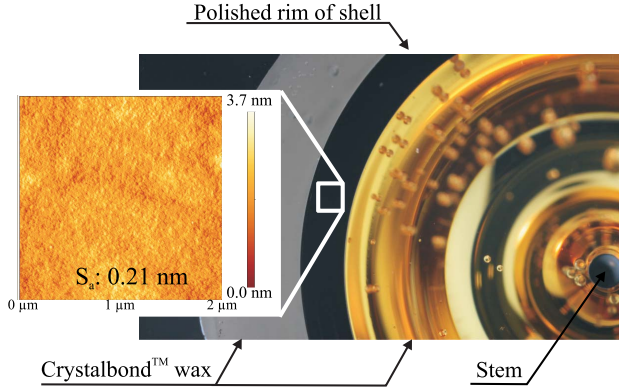

Fig. 20. The rim of shell was polished after removing the substrate. The AFM measurement on a sample area of 2 μm × 2 μm revealed a surface roughness of 0.21 nm.

n = 2 wineglass mode
Freq. = 22.24 kHz
τ = 13 s
Q = 0.91 million

n = 3 wineglass mode
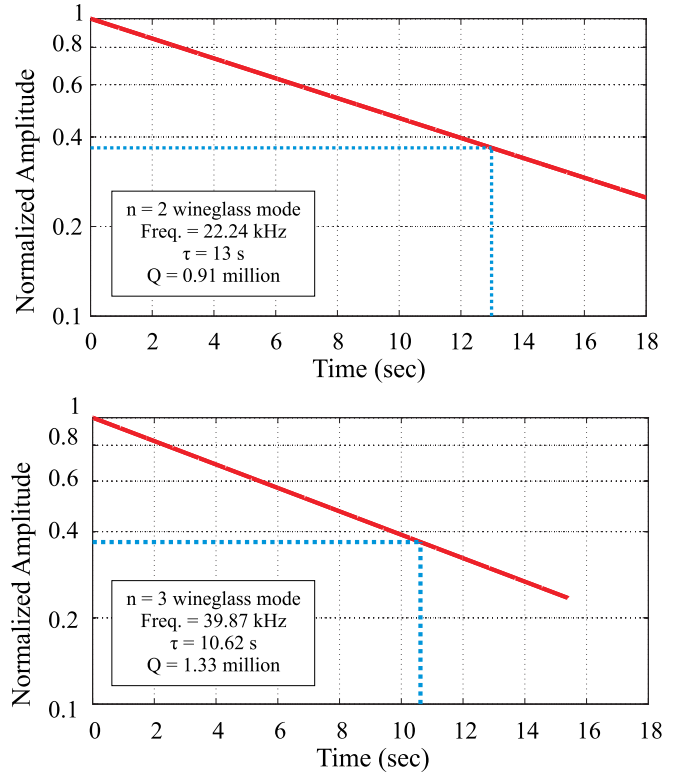Freq. = 39.87 kHz
τ = 10.62 s
Q = 1.33 million

Fig. 21. Decay time constant of a micro-shell resonator fabricated using the reverse cavity glassblowing process revealed the Q-factor of over 0.9 million in n=2 (top) and 1.33 million in n=3 (bottom) modes, measured at 20 μTorr. The shell diameter was 7 mm with an initial device thickness of 220 μm.

TABLE II

COMPARISON BETWEEN MEASUREMENT AND FE RESULTS OF
WINEGLASS FREQUENCIES AND Q-FACTORS
OF 220 μM DEVICE IN FIG. 18

	Axis	Freq. (kHz) (measurement)	Freq. (kHz) (simulation)	Q-factor (measurement)	Q-factor (TED)
n=2	X	22.24	19.49	0.91 M	2.6E8
	Y	22.22		0.9 M	
n=3	X	39.92	40.31	1.3 M	9.6E8
	Y	39.87		1.33 M	

before annealing

Q = 1.2 million
f = 21.8 kHz

τ = 17.6 seconds

after annealing

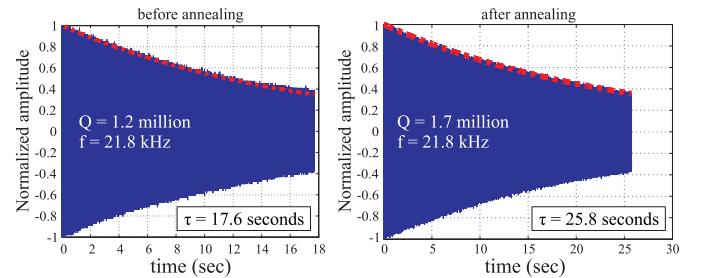Q = 1.7 million
f = 21.8 kHz

τ = 25.8 seconds

Fig. 22. Thermal annealing at 950 °C for 9 hours improved the Q-factor of a shell resonator from 1.2 million to 1.7 million. No significant change in the resonant frequency was observed.

The released shells were attached to a bulk piezo stack for an initial frequency response characterization. An AC signal was applied to the piezo stack, and the amplitude of vibration was measured using a Laser Doppler Vibrometer (LDV). After identification of resonant modes, the ringdown experiment was used to measure the energy decay time and the Q-factor of the fabricated shell resonators in a vacuum chamber. The Q-factor of 0.9 million was measured on the n=2 and 1.33 million on n=3 wineglass mode of an uncoated shell resonator at 20 μTorr, Fig. 21. The resonant frequency and the Q-factor of the degenerate wineglass modes of the shell are listed in Table. II. The as-fabricated frequency mismatch was 22 Hz and 48 Hz corresponding to n=2 and n=3 modes, respectively. Damping mismatch ($\Delta Q/Q$) less than two percent was measured between the degenerate wineglass modes. The comparison between the measured the Q-factor and the Q_{TED} of designed resonators revealed that the Q-factor was limited by other dissipation mechanisms. A non-isothermal and rapid cooling of glassblown shells would result in significant thermal stresses which increases the mechanical energy loss [29]. Optimal thermal annealing was demonstrated to improve the Q-factor by surface dehydroxylation and reduction of internal stresses [29]–[31]. A shell resonator with an initial Q-factor of 1.2 million was thermally annealed at 950 °C for 9 hours. The Q-factor was increased to 1.7 million after the thermal annealing, Fig. 22. Although the annealing process (temperature, duration, and cooling rate) was not optimized for size of the shell resonator, it provided an evidence that internal thermal stresses were developed in the shell during the glassblowing and cooling. Besides, surface dissipation due

to high surface to volume ratio and anchor losses due to unbalanced mass distribution in glassblown shells are other damping mechanisms that contribute to the overall Q-factor of shell resonators.

Lastly, the effect of shell geometric parameters on the modal frequency and ordering of the resonance modes were experimentally studied. The mode shape identification was performed using a servo-motor controlled rotary stage to
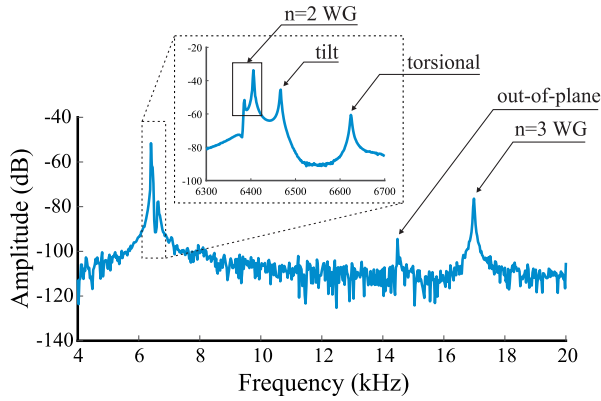
Fig. 23. An experimental frequency response of a shell resonator with the n=2 wineglass resonance at 6.4 kHz, showing a proximity of spurious resonance mode to the operational mode in a non-optimized design (thickness = 80 μm, shell radius = 5 mm, and anchor radius = 400 μm).
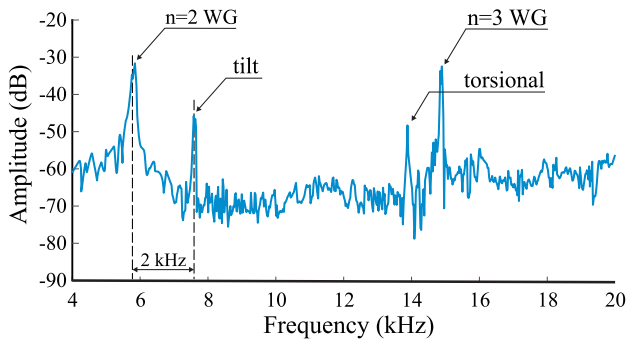

Fig. 24. A minimum frequency separation of 2 kHz was achieved between the n=2 wineglass and the closest resonance mode (tilt) in one of the design points, with thickness of 45 μm, shell radius of 4.25 mm, and anchor radius of 500 μm. The n=2 wineglass is the lowest resonance mode.

incrementally rotate the shell resonator with respect to the light source. A shell on a piezo stack was mounted on the rotary stage and the amplitude of vibration was measured using a Laser Doppler Vibrometer (LDV) at incrementally spaced azimuth angles at each peak frequency, to identify the corresponding mode shapes [32]. Fig. 23 shows the experimental frequency sweep response of a shell resonator, demonstrating a proximity of the resonance modes, less than 200 Hz between n=2 wineglass and the tilt mode in a non-optimized design.

The frequency response of a shell with thickness of 45 μm, shell radius of 4.25 mm, and anchor radius of 500 μm is shown in Fig. 24. The n=2 wineglass mode was identified at 5.7 kHz as the first vibration mode with a minimum frequency separation of 2 kHz to the nearest spurious mode (tilt). The experimental results demonstrated that frequency separation and mode-ordering could be achieved through parameters of shell geometry, at the operational frequency of interest.

VI. CONCLUSION

A comprehensive design and fabrication process of fused quartz hemi-toroidal shell resonators were presented. A design space for shell geometric parameters was constructed to increase the frequency separation between the n=2 wineglass operational mode and spurious modes. A possibility of ordering the resonance mode in the shell resonators only through the selection of proper geometric parameters was discussed and demonstrated. The dependency of Q_{TED} on the shell

geometry (thickness and diameter) were numerically analyzed. The presented procedure revealed that a mode-ordered shell resonator with a large operational/spurious frequency separation and high Q_{TED} could be achieved through the design of shell geometry. An example set of parameter for an operational frequency of 10 kHz was provided. A finite element method based on an iso-thermal fluid flow model was presented for the simulation of the glassblowing process. The simulations were used to determine the initial process parameters, and to predict the final geometry of the glassblown shells.

The limitations of the previously developed micro- glassblowing process, [13], were discussed and process modifications were proposed to enable fabrication of shell resonators with a broad range of thicknesses and diameters, resulting in realization of shell resonators with a wide range of operational frequencies. Mode-ordered shell resonators operating at 6 kHz were fabricated using the glassblowing process, validating the proposed design process for selection of parameters, and the proposed fabrication process to fabricate thin shell structures. The Q-factor of 1.7 million was demonstrated after thermal annealing of a shell resonators, revealing that internal residual stresses are most likely the limiting factor the overall Q-factor of the glassblown shell resonators.

The geometry optimization to achieve high Q-factor and larger separation between the operational and non-operational resonant modes were presented in this paper. Ultimately, for gyro implementation, other parameters such as effective mass, mechanical sensitivity, and detection efficiency must be optimized to improve the overall performance of micro-shell resonator gyroscopes [33], [34]. The developed micro glassblowing processes would enable a low-cost and highly-flexible fabrication of high-Q fused quartz micro shells which can be implemented as a core sensing element with a compact form factor in micro- resonators and Coriolis vibratory gyroscopes for precision navigation and timing applications.

REFERENCES

[1] D. M. Rozelle, "The hemispherical resonator gyro: From wineglass to the planets," in *Proc. 19th AAS/AIAA Space Flight Mech. Meeting*, Savannah, Georgia, Feb. 2009, pp. 1157–1178.

[2] P. Shao, C. L. Mayberry, X. Gao, V. Tavassoli, and F. Ayazi, "A polysilicon microhemispherical resonating gyroscope," *J. Microelectromech. Syst.*, vol. 23, no. 4, pp. 762–764, 2014.

[3] P. Pai, F. K. Chowdhury, C. H. Mastrangelo, and M. Tabib-Azar, "MEMS-based hemispherical resonator gyroscopes," in *Proc. IEEE SENSORS*, Taipei, Taiwan, Oct. 2012, pp. 1–4.

[4] Y. Xie, H.-C. Hsieh, P. Pai, H. Kim, M. Tabib-Azar, and C. H. Mastrangelo, "Precision curved micro hemispherical resonator shells fabricated by poached-egg micro-molding," in *Proc. IEEE SENSORS*, Taipei, Taiwan, Oct. 2012, pp. 1–4.

[5] D. Saito, C. Yang, A. Heidari, H. Najar, L. Lin, and D. A. Horsley, "Microcrystalline diamond cylindrical resonators with quality-factor up to 0.5 million," *Appl. Phys. Lett.*, vol. 108, no. 5, 2016, Art. no. 051904.

[6] N. Mehanathan, V. Tavassoli, P. Shao, L. Sorenson, and F. Ayazi, "Invar-36 micro hemispherical shell resonators," in *Proc. IEEE 27th Int. Conf. Micro Electro Mech. Syst.*, San Francisco, CA, USA, Jan. 2014, pp. 40–43.

[7] D. Senkal, M. J. Ahamed, A. A. Trusov, and A. M. Shkel, "Achieving Sub-Hz frequency symmetry in micro-glassblown wineglass resonators," *J. Microelectromech. Syst.*, vol. 23, no. 1, pp. 30–38, Feb. 2014.

[8] J. Giner, J. M. Gray, J. Gertsch, V. M. Bright, and A. M. Shkel, "Design, fabrication, and characterization of a micromachined glass-blown spherical resonator with insitu integrated silicon electrodes and ALD tungsten interior coating," in *Proc. 28th IEEE Int. Conf. Micro Electro Mech. Syst.*, Estoril, Portugal, Jan. 2015, pp. 805–808.

[9] B. Luo, J. Shang, Z. Su, J. Zhang, and C.-P. Wong, "Height adjustment of 3-D axisymmetric microumbrella shells for tailoring wineglass frequency," *IEEE Trans. Compon., Packag. Manuf. Technol.*, vol. 9, no. 3, pp. 567–574, Mar. 2019.

[10] B. Sarac, G. Kumar, T. Hodges, S. Ding, A. Desai, and J. Schroers, "Three-dimensional shell fabrication using blow molding of bulk metallic glass," *J. Micro-Electromech. Syst.*, vol. 20, no. 1, pp. 28–36, 2011.

[11] M. Kanik *et al.*, "Metallic glass hemispherical shell resonators," *J. Microelectromech. Syst.*, vol. 24, no. 1, pp. 19–28, Jan. 2015.

[12] D. Senkal, M. J. Ahamed, A. A. Trusov, and A. M. Shkel, "High temperature micro-glassblowing process demonstrated on fused quartz and ULE TSG," *Sens. Actuators A, Phys.*, vol. 201, pp. 525–531, Dec. 2012.

[13] D. Senkal, M. J. Ahamed, M. H. A. Ardakani, S. Askari, and A. M. Shkel, "Demonstration of 1 millionQ-factor on microglass-blown wineglass resonators with out-of-plane electrostatic transduction," *J. Microelectromech. Syst.*, vol. 24, no. 1, pp. 29–37, Feb. 2015.

[14] J. Y. Cho, J.-K. Woo, J. Yan, R. L. Peterson, and K. Najafi, "Fused-silica micro birdbath resonator gyroscope (μ-BRG)," *J. Microelectromech. Syst.*, vol. 23, no. 1, pp. 66–77, Feb. 2014.

[15] W. Li *et al.*, "Application of micro-blowtorching process with whirling platform for enhancing frequency symmetry of microshell structure," *J. Micromech. Microeng.*, vol. 28, no. 11, 2018, Art. no. 115004.

[16] E. J. Eklund and A. M. Shkel, "Glass blowing on a wafer level," *J. Microelectromech. Syst.*, vol. 16, no. 2, pp. 232–239, Apr. 2007.

[17] E. J. Eklund, A. M. Shkel, S. Knappe, E. Donley, and J. Kitching, "Glass-blown spherical microcells for chip-scale atomic devices," *Sens. Actuators A, Phys.*, vol. 143, no. 1, pp. 175–180, 2008.

[18] R. M. Noor, N. Kulachenkov, M. H. Asadian, and A. M. Shkel, "Study on Mems glassblown cells for NMR sensors," in *Proc. IEEE Int. Symp. Inertial Sensors Syst.*, Naples, FL, USA, Apr. 2019, pp. 1–4.

[19] I. P. Prikhodko, S. A. Zotov, A. A. Trusov, and A. M. Shkel, "Microscale glass-blown three-dimensional spherical shell resonators," *J. Micromech. Syst.*, vol. 20, no. 3, pp. 691–701, Jun. 2011.

[20] S. A. Zotov, I. P. Prikhodko, A. A. Trusov, and A. M. Shkel, "3-D micromachined spherical shell resonators with integrated electromagnetic and electrostatic transducers," in *Proc. Solid-State Sensors, Actuat., Microsyst. Workshop*, Hilton Head Island, SC, USA, Jun. 2010, pp. 11–14.

[21] M. H. Asadian, Y. Wang, and A. M. Shkel, "Design and fabrication of 3D fused quartz shell resonators for broad range of frequencies and increased decay time," in *Proc. IEEE SENSORS*, New Delhi, India, Oct. 2018, pp. 1–4.

[22] Y. Wang, M. H. Asadian, and A. M. Shkel, "Modeling the effect of imperfections in glassblown micro-wineglass fused quartz resonators," *J. Vib. Acoust.*, vol. 139, no. 4, 2017, Art. no. 040909.

[23] D. Vatanparvar and A. M. Shkel, "Effect of fabrication imperfections on energy loss through mechanical mode coupling in MEMS," in *Proc. IEEE Int. Symp. Inertial Sensors Syst.*, Lake Como, Italy, Mar. 2018, pp. 1–2.

[24] C. Zener, "Internal friction in solids II. General theory of thermoelastic internal friction," *Phys. Rev. J. Arch.*, vol. 53, no. 1, p. 90, 1938.

[25] R. Lifshitz and M. L. Roukes, "Thermoelastic damping in micro-and nanomechanical systems," *Phys. Rev. B, Condens. Matter*, vol. 61, no. 8, p. 5600, 2000.

[26] A. Darvishian, T. Nagourney, J. Y. Cho, B. Shiari, and K. Najafi "Thermoelastic dissipation in micromachined birdbath shell resonators," *J. Microelectromech. Syst.*, vol. 26, no. 4, pp. 758–772, Aug. 2017.

[27] M. H. Asadian, Y. Wang, S. Askari, and A. Shkel, "Controlled capacitive gaps for electrostatic actuation and tuning of 3D fused quartz micro wineglass resonator gyroscope," in *Proc. IEEE Int. Symp. Inertial Sensors Syst.*, Kauai, HI, USA, Mar. 2017, pp. 1–4.

[28] R. H. Doremus, "Viscosity of silica," *J. Appl. Phys.*, vol. 92, no. 12, pp. 7619–7629, 2002.

[29] B. S. Lunin and K. V. Tokmakov, "Reduction in internal friction in silica glass with high OH content," *J. Amer. Ceram. Soc.*, vol. 102, no. 6, pp. 3329–3340, 2018.

[30] B. Lunin, A. Kharlanov, and S. Kozlov, "Dehydroxylation and formation of KU-1 silica glass surface defects during annealing," *Moscow Univ. Chem. Bull.*, vol. 65, no. 1, pp. 34–37, 2010.

[31] A. Ageev, B. C. Palmer, A. De Felice, S. D. Penn, and P. R. Saulson, "Very high quality factor measured in annealed fused silica," *Classical Quantum Gravity*, vol. 21, no. 16, p. 3887, 2004.

[32] Y. Wang, M. H. Asadian, and A. M. Shkel, "Compensation of frequency split by directional lapping in fused quartz micro wineglass resonators," *J. Micromech. Microeng.*, vol. 28, no. 9, 2018, Art. no. 095001.

[33] W. Li *et al.*, "A novel high transduction efficiency micro shell resonator gyroscope with 16 T-shape masses using out-of-plane electrodes," *IEEE Sensors J.*, vol. 19, no. 13, pp. 4820–4828, Jul. 2019.

[34] D. Xiao *et al.*, "Fused silica micro shell resonator with T-shape masses for gyroscopic application," *J. Microelectromech. Syst.*, vol. 27, no. 1, pp. 47–58, Feb. 2018.

Mohammad H. Asadian (S'15) received the B.S. and M.S. degrees in mechanical engineering from the Amirkabir University of Technology (Tehran Polytechnic), Tehran, Iran, in 2007 and 2010, respectively, and the M.S. and Ph.D. degrees in mechanical and aerospace engineering from the University of California, Irvine, CA, USA, in 2017 and 2019, respectively. His current interests include design, modeling, and control of MEMS inertial sensors and systems for navigation applications.

Yusheng Wang received the B.Eng. degree (Hons.) in engineering mechanics from Tsinghua University, Beijing, China, in 2014, and the M.S. degree in mechanical engineering from the University of California, Irvine, CA, USA, in 2016. He is currently pursuing the Ph.D. degree with Microsystems Laboratory, University of California, Irvine, CA, USA. His research interests include design, analysis, fabrication, and post-processing of 3-D micromachined resonators, and aided inertial navigation algorithm development. He is a recipient of the 2016-2017 Paul and Beverly Holmes Fellowship and the Best Student Paper Award at the IEEE Inertial 2019. He serves as a Reviewer for JMEMS, JMEMS Letters, and Sensors Letters.

Andrei M. Shkel (F'99) received the Diploma degree (Hons.) in mechanics and mathematics from Moscow State University, Moscow, Russia, in 1991, and the Ph.D. degree in mechanical engineering from the University of Wisconsin-Madison, Madison, WI, USA, in 1997. In 2000, he joined the faculty of the University of California at Irvine, Irvine, CA, USA, where he is currently a Professor with the Department of Mechanical and Aerospace Engineering, with joint appointments in the Department of Electrical Engineering and Computer Science and the Department of Biomedical Engineering. He has served as the Program Manager of the Microsystems Technology Office, Defense Advanced Research Projects Agency, Arlington, VA, USA, from 2009 to 2013. His professional interests are reflected in over 250 publications. He holds over 40 U.S. patents. His current interests include the design, manufacturing, and advanced control of precision micromachined gyroscopes. He was a recipient of the 2002 George E. Brown, Jr., Award, the 2005 NSF CAREER Award, the 2006 UCI HSSoE Best Faculty Research Award, the 2009 IEEE Sensors Council Technical Achievement Award, and the 2019 Innovator Award. In 2013, he received the Office of the Secretary of Defense Medal for Exceptional Public Service. He has served on a number of editorial boards, most recently, as an Editor of the IEEE/ASME JOURNAL OF MICROELECTROMECHANICAL SYSTEMS, an Associate Editor-in-Chief of the IEEE SENSORS LETTERS, an Editorial Board Member of the Journal of Gyroscopy and Navigation, and the Founding Chair of the IEEE International Symposium on Inertial Sensors and Systems. He was voted the 2018 President-Elect of the IEEE Sensors Council.